Diffuse back-illumination setup for high temporally resolved extinction imaging

Westlye, Fredrik Ree; Penney, Keith; Ivarsson, Anders; Pickett, Lyle M.; Manin, Julien; Skeen, Scott A.

Published in:
Applied Optics

Link to article, DOI:
10.1364/AO.56.005028

Publication date:
2017

Document Version
Publisher's PDF, also known as Version of record

applied optics

Diffuse back-illumination setup for high temporally resolved extinction imaging

Fredrik R. Westlye,[1,*] Keith Penney,[2] Anders Ivarsson,[1,3] Lyle M. Pickett,[2] Julien Manin,[2] and Scott A. Skeen[2,4]

[1]Department of Mechanical Engineering, Technical University of Denmark, Nils Koppels Allé Bld. 403, 2800 Kgs. Lyngby, Denmark
[2]Sandia National Laboratories, P.O. Box 969, Livermore, California 94550, USA
[3]e-mail: ai@mek.dtu.dk
[4]e-mail: sskeen@sandia.gov
*Corresponding author: frrwe@mek.dtu.dk

Received 18 April 2017; accepted 9 May 2017; posted 15 May 2017 (Doc. ID 293025); published 9 June 2017

This work presents the development of an optical setup for quantitative, high-temporal resolution line-of-sight extinction imaging in harsh optical environments. The application specifically targets measurements of automotive fuel sprays at high ambient temperature and pressure conditions where time scales are short and perceived attenuation by refractive index gradients along the optical path (i.e., beam steering) can be significant. The illumination and collection optics are optimized to abate beam steering, and the design criteria are supported by well-established theoretical relationships. The general effects of refractive steering are explained conceptually using simple ray tracing. Three isolated scenarios are analyzed to establish the lighting characteristics required to render the observed radiant flux unaffected by the steering effect. These criteria are used to optimize light throughput in the optical system, enabling minimal exposure times and high-temporal resolution capabilities. The setup uses a customized engineered diffuser to transmit a constant radiance within a limited angular range such that radiant intensity is maximized while fulfilling the lighting criteria for optimal beam-steering suppression. Methods for complete characterization of the optical system are detailed. Measurements of the liquid–vapor boundary and the soot volume fraction in an automotive spray are presented to demonstrate the resulting improved contrast and reduced uncertainty. The current optical setup reduces attenuation caused by refractive index gradients by an order of magnitude compared to previous high-temporal resolution setups.

OCIS codes: (110.0113) Imaging through turbid media; (110.0115) Imaging through turbulent media; (290.2200) Extinction.

https://doi.org/10.1364/AO.56.005028

1. INTRODUCTION

Line-of-sight extinction measurements aim to quantify the attenuation of light caused by absorption and scattering in fluids and particle (and/or droplet) -laden media. For the case of extinction by particles and droplets, the attenuation is commonly related to an optical thickness (KL) through the Beer–Lambert law [1]. Although extinction measurements are often simple and cost effective, as a line-of-sight diagnostic, their utility can be hampered by perceived attenuation caused by refractive index gradients (often referred to as beam steering). Beam steering can be severe in high-pressure, high-temperature environments common to real-world combustion applications, making it difficult to distinguish absorption- and/or scattering-induced attenuation from light loss caused by refractive index gradients. In the case of laser extinction measurements, attenuation by beam steering can be avoided by using a sufficiently large angular aperture on the collection side, as demonstrated by Musculus and Pickett [2]; however, for imaging applications, the requirements are more extensive and include attention to the characteristics of the illumination source.

There is a need for quantitative, high-temporal resolution imaging diagnostics amenable to the optically harsh environments encountered in high-pressure combustion applications. As will be discussed below, specific measurement targets include the transient liquid length and soot formation in fuel sprays. To meet this need, a diffused back-illumination extinction imaging (DBIEI) system, inspired by the Ghandhi and Heim [3] setup, has been used by a number of institutions participating in the Engine Combustion Network (ECN) [4–7]. DBIEI has been used to measure the liquid length of diesel sprays from a set of shared injectors. The DBI approach for liquid length measurements, referred to hereafter as DBIEI-LL, was suggested as an experimental standard for the ECN as opposed to Mie

scattering measurements, which can be difficult to quantify consistently among the participating institutions [5].

With regard to soot quantification, the same optical approach has been used to measure the time-resolved optical thickness of high-pressure combusting sprays at rates exceeding 40 kHz [6,8,9]. This high-speed DBI soot extinction imaging (DBIEI-soot) diagnostic proved to be a simple and cost-effective approach for quantifying soot at speeds exceeding those achieved by high-speed planar laser-induced incandescence (PLII) [10–12]. Moreover, DBIEI-soot can successfully quantify soot in flames where the optical thickness exceeds KL = 2—a limitation for PLII due to high attenuation of the incident laser sheet as demonstrated by Pickett and Siebers [13,14]. High-speed PLII also risks becoming intrusive when the laser fluence approaches the plateau regime. Sjöholm [10] observed a 30% reduction in signal at a repetition rate of only 50 Hz (20-ms pulse separation time) due to particle sublimation. Ultimately, Bakker [12] concluded that PLII is feasible only if the laser fluence is kept well below the plateau regime, further restricting its usefulness in optically thick environments such as those found in combusting diesel sprays. In contradistinction, DBIEI-soot is completely non-intrusive, and optical thicknesses exceeding KL = 4 are feasible based on modern CMOS camera signal-to-noise ratio characteristics.

In spite of the benefits of DBIEI as a line-of-sight technique, this optical configuration also comes with drawbacks. Obviously, this requires optical access that may be unavailable or severely limited in reciprocating engines. Furthermore, the most accurate tomographic reconstruction of the instantaneous f_v would require simultaneous acquisition of line-of-sight data from multiple angles. Another weakness related to the line-of-sight arrangement is the potential for error due to apparent attenuation induced by refractive index gradients (i.e., beam steering), as mentioned in the introduction. The severity of beam steering increases dramatically at higher ambient pressures. Steep refractive index gradients are not only observed at the boundary of a high-temperature combusting fuel spray, but can be observed near the liquid boundary of a non-reacting spray where the fuel vapor is cooler than the ambient gases. Thus, DBIEI, as it has been previously demonstrated in the literature [5,6,9,15], is subject to uncertainties caused by beam steering. The purpose of the present work is to lay out an optical arrangement that eliminates quantitative uncertainties in liquid boundary and soot measurements induced by beam steering when applying DBIEI. It should be mentioned that this measurement technique is not limited only to automotive fuel spray applications, but general to all applications involving imaging of extinction in the presence of steep refractive gradients.

2. DIFFUSED LIGHTING TO MINIMIZE BEAM-STEERING EFFECTS

An ideal diffused light source has constant radiance-emitting light at all forward angles and is commonly referred to as a Lambertian emitter. The observed radiant flux (Φ_{obs}) from an extended Lambertian emitter, immersed in surroundings with the same refractive index, is independent of the viewing angle and distance from the emitter. It depends only on the radiance emitted by the source (L_{em}), the solid angle subtended by the angular aperture of the collection optics, and the area of the observer (A_{obs}) (e.g., the area of a pixel) as defined in Eq. (1) (cf. Appendix A). The term "extended" is used here to define that the emitting surface is larger than the area subtended by the collection system,

$$\Phi_{obs} = L_{em}\dot{\Omega}_{obs}\dot{A}_{obs}. \quad (1)$$

As demonstrated by shadowgraphy or schlieren imaging, beam steering can cause a reduction or an increase in the observed radiant flux when rays from the source are refracted or "steered" outside the collection cone defined by the angular aperture, or when rays originally outside the collection cone are steered in. However, if the illumination source is sufficiently extended, spatially uniform, and Lambertian, any light ray steered away from its initial trajectory by refraction will be replaced by another ray of equal radiance from the source.

To illustrate this concept, we consider three major refractive effects that may be encountered. For demonstration purposes, the effects are discussed independently; however, in a real system with a complex distribution of refractive index gradients, these effects may occur in combination.

The three major refractive effects discussed here include rays passing through (a) parallel-faced, (b) non-parallel-faced, and (c) non-planar refracting media. The illustrations in Fig. 1 represent the light path described by the chief and marginal rays from the detector point of view. The resulting plots are based on sequential ray tracing of the light collected by a specific pixel on the imaging sensor. For visual simplicity, the illustrations are in 2D with the acceptance cone being rotationally symmetric around the chief ray, with Ω_{obs}, θ, and A_{obs} being the solid angle, viewing angle, and the area of the projected pixel of the un-refracted acceptance cone, respectively. The prime denotes the same parameters belonging to the refracted acceptance cone.

Figure 1(a) shows rays traced through a parallel-faced refracting medium. It is seen that the acceptance cone that collects light from the source may be translated spatially in any of the x and y directions depending on the orientation of the refracting medium. The light collection system will therefore collect a bundle of rays from a different location on the extended source relative to the un-refracted case. However, all the parameters determining the observed radiant flux [Eq. (1)] are consistent: $\theta = \theta'$, $\Omega_{obs} = \Omega'_{obs}$, and $A_{obs} = A'_{obs}$. As long as the size of the source is sufficiently large and its radiance spatially uniform, the radiant flux observed by the pixel will remain unchanged.

For the case of a non-parallel-faced refracting medium depicted in Fig. 1(b), the refracted acceptance cone is both translated and rotated. This results in a refracted viewing angle, θ', that is no longer perpendicular to the source. The solid angle and projected pixel area of the refracted acceptance cone remain unaltered, that is, $A_{obs} = A'_{obs}$ and $\Omega_{obs} = \Omega'_{obs}$, respectively. Requirements to the size and spatial uniformity of the source still apply; however, the altered viewing angle, $\theta \neq \theta'$, also requires that the angular distribution of radiance from the source be uniform to observe a constant radiant flux. Alternatively, the same can be achieved if the angular distribution is small relative to Ω_{obs}.

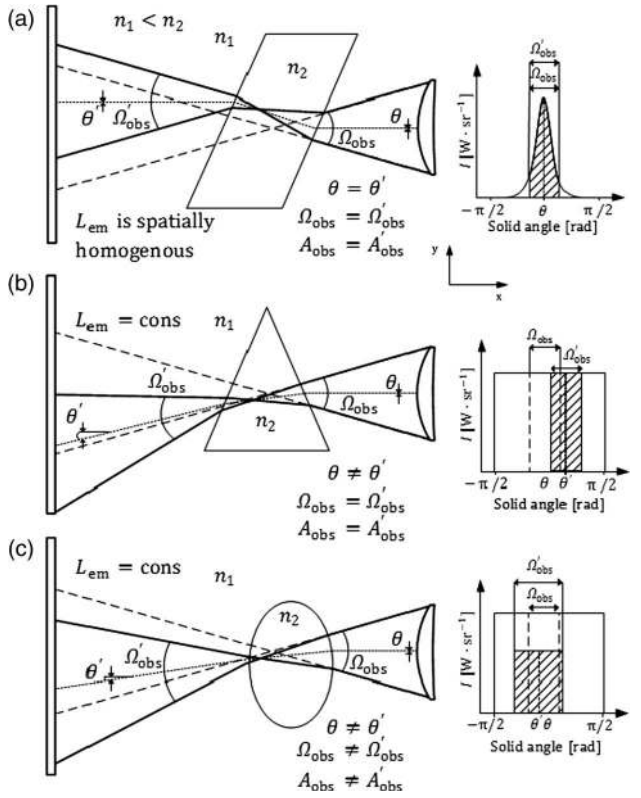

Fig. 1. Illustrations of acceptance cones collecting light to a specific pixel on an imaging sensor. Chief and marginal rays are traced through (a) parallel-faced, (b) non-parallel-faced, and (c) non-planar-faced refracting media. The solid lines trace the refracted marginal rays, the dashed lines the un-refracted marginal rays, and the dotted line shows the refracted chief ray. The plot to the right illustrates the angular distribution of radiant intensity, and the shaded area represents the radiant flux received by the pixel.

Figure 1(c) shows that a refracting medium with non-planar surfaces alters the solid angle of the refracted collection cone and the projected pixel size ($\Omega_{obs} \neq \Omega'_{obs}$ and $A_{obs} \neq A'_{obs}$), in addition to the translation and rotation observed in the previous example. However, conservation of energy in an ideal optical system requires that the product of the observed area and the observed solid angle is constant when the observer and emitter are in surroundings with equal refractive index (cf. Appendix A). Thereby $\Omega_{obs}A_{obs} = \Omega'_{obs}A'_{obs}$. This special case of optical invariant is also known as the Gaussian lens equation. Thus, the source must be extended, spatially uniform, and of constant radiance. Under these constraints, the optical invariant ensures that non-parallel refracting media will not alter the detected radiant flux.

In summary, to counteract translation, rotation, and altered solid angle of the acceptance cone from refraction interactions, the criteria for the illumination source are (1) the source should be sufficiently extended beyond the area observed by the optical sensor (a pixel), and (2) the source should emit light with constant radiance within all angles that may be collected to the sensor and within the extent they may be steered. If these criteria are fulfilled, only other attenuation processes such as absorption and scattering can reduce the observed radiant flux. It must be noted, however, that a remaining consequence of refractive effects is the degradation of spatial resolution in an extinction imaging setup. This degradation is mainly due to varying depth of field and displacement around the focal plane, ultimately integrated onto the pixel. The magnitude of the degradation is dependent on the direction and steepness of the refractive gradients.

A. Review of Previous Optical Solutions for Extinction Imaging

A light source for image-based extinction measurements that complies perfectly with the criteria summarized in the previous section is difficult to obtain in reality. A handful of prior studies have used image-based extinction methods with different optical arrangements and various degrees of success. Samples of the most relevant optical arrangements are shown in Fig. 2 [3,16–18]. These setups had different objectives and constraints, but relied on light attenuation from scattering and/or

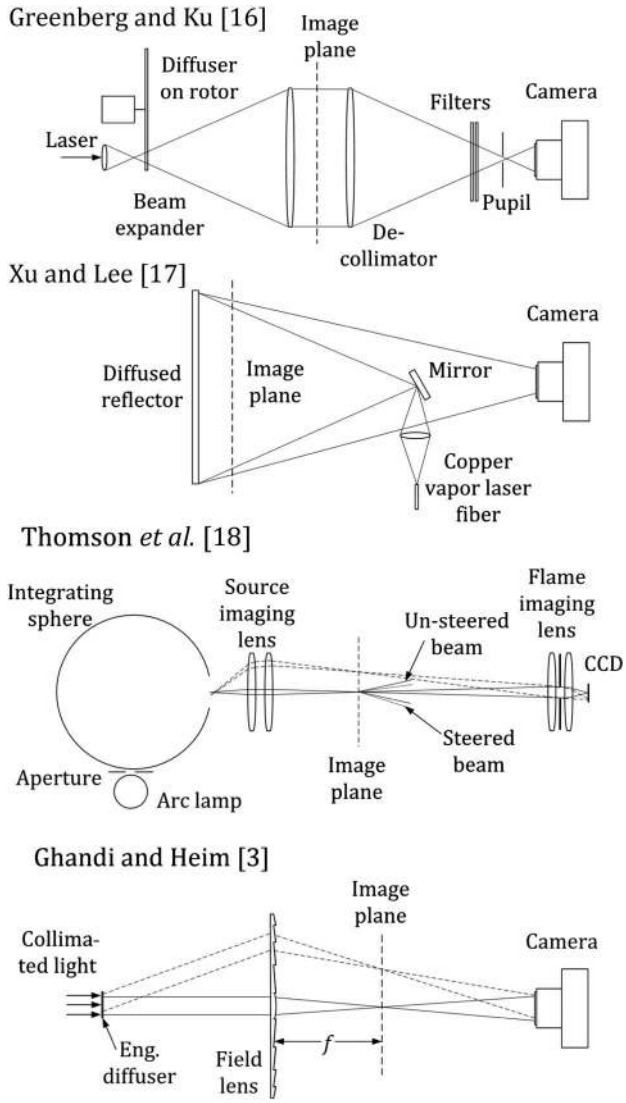

Fig. 2. Schematics of previous optical setups for extinction imaging [16,17,18,3].

absorption to quantify optical extinction. A brief description of the setups is given below along with key performance parameters.

In the setup at the top of Fig. 2, Greenberg and Ku [16] expanded a laser to image soot extinction in a laminar diffusion flame at atmospheric pressure. The diverging laser passed through a rotating diffuser to "minimally de-collimate" the beam and eliminate speckle, which occurs due to the coherent nature of laser light. The de-collimated light was then collected by a large lens and transmitted through the test section (i.e., the flame). The transmitted light was refocused by another large lens (de-collimator) and imaged directly onto the camera sensor after passing through a narrow aperture and a camera objective. Because the light rays remain fairly collimated in this setup, this arrangement is more susceptible to beam-steering artifacts.

Xu and Lee [17] used a diffuse reflector behind the image plane to build a forward-illuminated setup. In such a configuration, the laser light source and the light collection are located on the same side of the flame for applications having only a single optical access. In this method, the light must pass through the attenuating media twice—once as an expanding laser beam and a second time as the reflected diffuse light. This doubling of optical length will reduce the method's applicability under more optically thick conditions. Another drawback of the method is that the uniformity of the light incident on the diffuser (and therefore reflected by the diffuser) will be influenced by beam steering of the expanded laser on its first pass through the attenuating media.

Thomson *et al.* [18] used an arc lamp coupled to an integrating sphere as a light source for diffused back-illuminated imaging of soot extinction. In that setup, the Lambertian output in the port of the integrating sphere was imaged in the center of the flame. The angular intensity distribution in this plane depends on the angular aperture of the source imaging lenses and was found to be approximately 20 deg. based on ray-tracing simulations of the setup using commercially available software (Zemax). As shown in Fig. 3, ray tracing also indicates that the angle of the optical axis is offset in the periphery due to the spherical nature of the lenses. This is of course also the case for the flame imaging lenses. As the source is imaged onto the image plane, the angle of the optical axis is offset in the opposite direction relative to that of the flame imaging lenses. For this reason, the angular aperture of the flame imaging lens was purposely much smaller than that of the source imaging lens, such that its view always fell within the aperture of the source imaging lens as seen in Fig. 2. With this small angular aperture, the radiance in the image plane was sufficient to suppress beam-steering effects in a laminar diffusion flame at an ambient pressure of 10 atm. For high-temporal resolution applications, however, the overall light transmission efficiency of this setup would be insufficient. This is attributable to reflection losses in the integrating sphere and the small angular aperture of the source-imaging lens. Non-sequential ray-tracing calculations found the light throughput to the image plane to be on the order of 1.7%. Further, only a fraction of this light will be imaged onto the detector due to the small angular aperture requirement of the flame-imaging lenses.

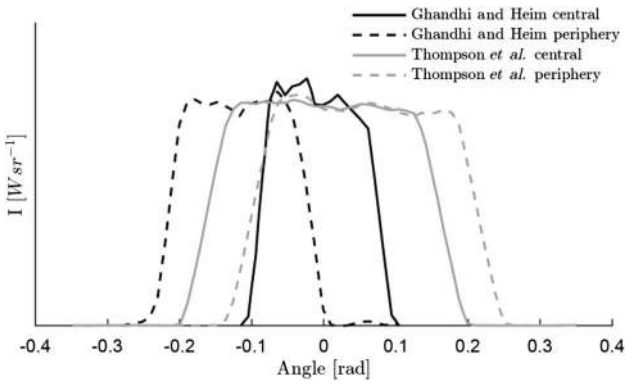

Fig. 3. Angular distribution in image plane of the Ghandhi and Heim and Thomson *et al.* optical setups as calculated with non-sequential ray tracing using commercial software ZEMAX. Y-axis values are not representative, as the results have been scaled for comparison.

To enhance light throughput relative to prior techniques for applications requiring high-temporal resolution, Ghandhi and Heim [3] used a small (25 mm) engineered diffuser to generate a specified output radiant intensity distribution from a collimated input. The diffused light was collected by a large Fresnel lens and redirected through the region of interest toward the collection optics. The setup was dimensioned such that the imaging optics would always see a select portion of the light emitted from the diffuser through the Fresnel lens. With the image plane located at the focal distance of the Fresnel lens, the camera collects a narrow angular portion of the radiance emitted from a large area on the diffuser. The spatial intensity distribution then translates into the angular distribution in the image plane, requiring spatial uniformity across the diffuser, as seen in Fig. 2. In this configuration, the angular distribution in the image plane depends largely on the size of the diffuser, the distances between optical components, and the spatial uniformity of the output from the diffuser. Ghandhi and Heim found that this setup yielded an optical efficiency more than two orders of magnitude higher than a conventional flood illumination system. A ray-tracing simulation of the Ghandhi and Heim setup (152.4 mm $f/1$ Fresnel lens, 25.4 mm 50 deg. diffuser) yields a 0.18-rad or 10-deg. angular intensity distribution in the image plane (Fig. 3). The distribution is narrower than that of the Thompson *et al.* setup [18], and the angle of the optical axis in the periphery is offset in the opposite direction, thus following that of the collection.

Leveraging its superior optical efficiency, a modified version of the Ghandi and Heim [5,6,8,15] setup has been successfully employed in the ECN community for extinction measurements of sprays and spray flames in high-pressure and high-temperature environments. This setup replaced the collimated source of Ghandi and Heim with high-intensity pulsing LEDs to achieve high-temporal resolution without the cost and complexity of a pulsed/burst laser. The Sandia-developed LED driver [19] is capable of generating short (below 10 ns), intense light pulses (over 100 W peak optical power), enabling improved visualization of fast-moving (>100 m/s) spray structures [20]. Moreover, the low cost of the driver and LEDs relative to high-repetition-rate lasers makes such a configuration amenable to standardization and widespread usage within the

ECN community and beyond. As will be discussed in more detail later, however, the modified Ghandi and Heim setup does not fully mitigate beam-steering artifacts due the use of a non-collimated light source as input to the engineered diffuser. Furthermore, a detailed description of the illumination requirements for a standardized and generally applicable optical configuration has not yet been provided. For this reason, a better understanding of the refractive effects in conjunction with methods for characterization and standardization of the technique is desired in the ECN community.

In summary, each diffused back-illuminated technique described above can be used for two-dimensional extinction measurements under certain conditions with all but the Ghandi and Heim type method restricted to steady-state or low-temporal resolution systems. The remainder of the present work presents the development and characterization of a robust, standardized, high-temporal resolution imaging extinction diagnostic. In particular, we present measurements of the spatial uniformity and angular distribution of the illumination at the image plane and describe the illumination and collection requirements that must be met to suppress beam steering in an imaging extinction setup.

3. DIMENSIONING DBI SETUP WITH HIGH-TEMPORAL RESOLUTION CAPABILITIES

High-temporal resolution imaging systems require an intense light source to make full use of the sensor's dynamic range despite an inherently short exposure time. For a light source with a fixed output power, maximal temporal resolution is achieved by minimizing light losses between the source and collection optics. In a typical imaging system, the angular aperture of the collection lens will be much smaller than the angular distribution of light from an extended Lambertian source. Thus, only a fraction of the light from such a source would be directed into the angular aperture of the collection lens, and maximum temporal resolution would be compromised. It is therefore desirable to have a spatially uniform extended illumination source that emits uniform radiance only within a specified solid angle. This can be achieved with a large-area engineered diffuser combined with the appropriate input illumination. The remainder of this section outlines the necessary steps to optimally dimension and characterize a diffused back-illumination imaging system.

In Fig. 4, we provide a general representation of an extended illumination source with a specified angular range (β) of "cropped" Lambertian illumination and a light collection system characterized by an angular aperture (ω). Here, D is the extent of the source, L is the distance from the source to the imaging plane, S is the size of the image plane, and O is the distance from the camera lens to the image plane. From the refractive steering scenarios mentioned above, it can be seen that the radiance needs to be constant only in the range $\omega + 2\zeta$, where 2ζ is the magnitude of full angle beam steering that can be expected. As the engineered diffuser is flat and orthogonal to the optical axis, the $\omega + 2\zeta$ criterion is valid only in the center of the image or if the collection optics are telecentric. For conventional lenses, the optical axis is not normal to the source in the periphery of the view field. To account

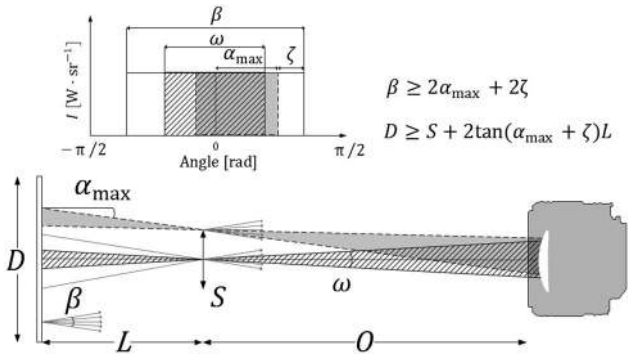

Fig. 4. DBI illumination setup optimized for high-temporal resolution capabilities.

for this, the source should have a constant radiance in the range $2\alpha + 2\zeta$, where α is the angle formed between the steepest ray collected by the lens and a vector normal to the source emission plane, which has its maximum (α_{max}) in the periphery of the image plane, $S/2$, as shown in Fig. 4.

It is recognized that the physical dimensions of a given optically accessible experimental system may constrain the distance between the engineered diffuser and the image plane (L), the distance from the image plane to the collection lens (O), and the diffuser size (D). This is especially true in closed systems such as vacuum chambers or high-pressure vessels where optical window position and aperture are fixed. Ultimately, the minimum required angular range, β, of constant radiance depends on the choice and position of the collection optics. All relevant dimensions to specify the optical setup are noted in Fig. 4, and the methodology used to characterize ω, α, and L_{em} is detailed in the next section.

4. CHARACTERIZATION OF LIGHTING AND COLLECTION OPTICS

The lighting requirements specified in the previous section are coupled to the collection optics' characteristics. For variable-focus objective lenses, the definition of the f-number (N) as the ratio of the focal length to the entrance pupil ($N = f/E_N$) is valid only at infinite focus. As the focal plane moves closer to the objective, the effective f-number increases [21]. Because the f-number defines the angular aperture of the optic, it should be measured for the objective exactly as it will be used in the designed setup as a camera-lens system. An objective lens can be characterized by focusing on a Lambertian source (e.g., the output plane of a large-area integrating sphere) at the distance corresponding to the experimentally constrained focal plane. A band-pass filter should be placed in front of the source to minimize chromatic aberrations, and a non-reflective horizontal ~5 mm slit should be placed directly in front of the lens to ensure a 2D measurement.

The location of the marginal rays (thereby also the chief ray) of the central acceptance cone can then be identified by moving a non-reflective cropping tool horizontally along the face of the slit, from both sides individually, while monitoring the intensity of the sensor's central pixel(s). When the pixel intensity falls

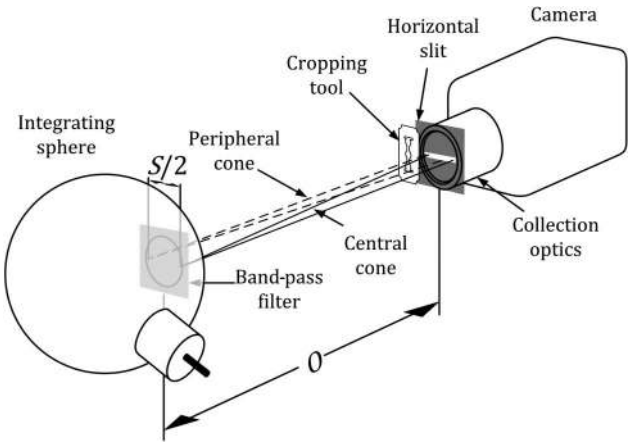

Fig. 5. Illustration of camera objective characterization. Chief and marginal rays of the acceptance cone to a central (solid) and peripheral (dotted) pixel are shown.

below a predefined threshold, the marginal rays of the collection cone are being cropped, and their positions at the lens face are thus identified (Fig. 5). It is recommended that the camera's full dynamic range be utilized, without saturation, to maximize the sensitivity of the measurement. The same procedure is repeated for the outermost peripheral pixel in the same row as the central pixel. The corresponding collection angles are then determined through simple trigonometry using the distances measured at the lens face.

A 50 mm $f/1.2$ lens objective equipped with a two-diopter close-up lens has been used in this work. Measurements of α and ω for this lens combination are provided in Fig. 6.

The first lens element of the collection optics was 233 mm from the image plane ($O = 233$ mm) with the diffuser further removed by 100 mm ($L = 100$ mm). At the selected resolution (640 × 304 pixels), the width of the image plane field of view was $S \approx 60$ mm yielding a measured α_{max} of ~9.8 deg. From these measurements, one can deduce that for a specific point in the object plane, beam steering is sufficiently mitigated if $\beta \geq 2(\alpha + \zeta)$. If $2(\alpha + \zeta) > \beta \geq 2\alpha$, light will be steered only out of the acceptance cone. If $\beta < 2\alpha$, light will be steered both into and out of the acceptance cone. This is illustrated in Fig. 7.

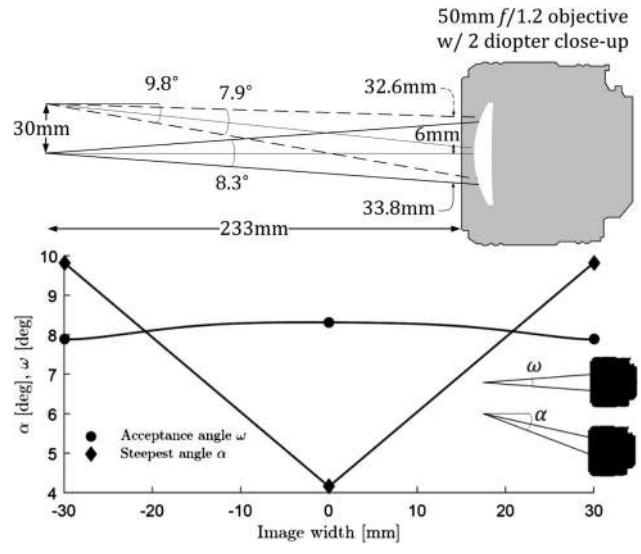

Fig. 6. Measured acceptance angle ω and steepest angle α (bottom) at various points in the image plane with a 50 mm $f/1.2$ lens objective equipped with a two-diopter close-up lens. The corresponding angles are illustrated in the top figure and indicated in the insets on the plot. The measurements used a 1% decrease in pixel count threshold.

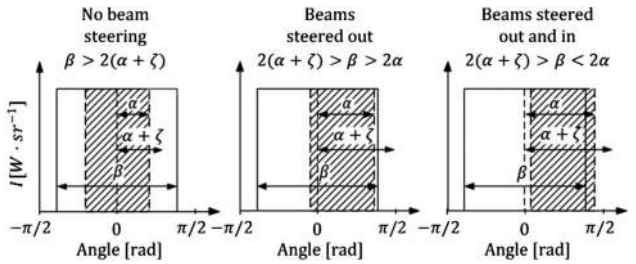

Fig. 7. Illustration demonstrating how beam steering can potentially induce an apparent optical thickness. Beams being steered out induce a positive optical thickness, while beams being steered in induce a negative optical thickness.

Because ζ is a property of the flame, the apparent optical thickness resulting from beam steering is potentially higher when ω is small relative to ζ. For example, if ω is smaller than ζ, all the light can potentially be steered out of the acceptance cone, resulting in an apparent optical thickness of ∞. For this reason, it is beneficial to use a low f-number objective.

The quantity 2ζ has been investigated in high-pressure combusting automotive sprays and represents a relatively extreme manifestation of beam steering in combustion systems [2]. The study measured the extinction of a HeNe laser (635 nm) passing through a flame in a high-pressure, high-temperature combustion chamber. The magnitude of beam steering was determined by measuring how much of the signal was clipped while varying the size of an aperture. It was found that 95% of beam steering occurred within 50 mrad full angle corresponding to 2.86° [2]. With this quantity, the engineered diffuser should have a full diffusing angle of ~22°, and the relations presented in Section 3 above (see Fig. 4) require the size of the engineered diffuser to be $D \geq 105$ mm when placed 100 mm from the focal plane.

The engineered diffusers used in this work are refractive diffusers and require a collimated light input. The output radiance is affected by the degree of collimation, spatial uniformity, and the wavelength of incident light. The source should also be incoherent as a coherent input produces speckle. Generating a large, perfectly collimated beam of incoherent light without sacrificing light throughput is no trivial task. Therefore, the radiance output from the engineered diffuser should be characterized for the specific optical arrangement. In this work, an LED source was used. The driver technology developed by our group can generate intense, spectrally narrow light with short pulse durations [19]. In pulsing mode, the light intensity can reach an order of magnitude higher than in continuous-wave mode, allowing the LED driver to replace a high-speed laser system in certain applications at a fraction of the cost. The collimated beam to the engineered diffuser was generated by a

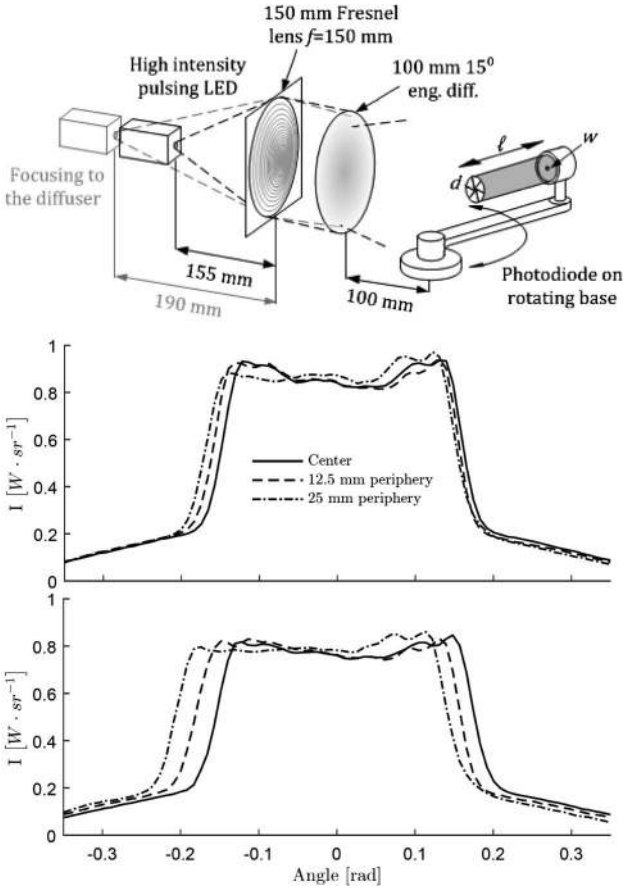

Fig. 8. (Top) Specific optical arrangement used to generate the input to the large engineered diffuser. Also shown is the radiance measurement technique used to characterize the lighting. (Middle) Measured angular intensity distribution at three locations across the imaging plane with collimated input to the diffuser. (Bottom) Measured angular intensity distribution at three locations across the imaging plane with a slightly focused input to the diffuser.

623-nm, single-dye, SSR-90 3 × 3 mm Luminous LED placed one focal distance away from a 150 mm $f/1$ Fresnel lens. The lighting has been characterized across the image plane by a 1D measurement using a small-area photo diode (1 × 1 mm) on a rotating arm as shown in Fig. 8 (top). A variable aperture with diameter d mounted a distance, ℓ, away from the sensor will adjust the angular resolution of the measurement through Eq. (2):

$$R = 2\tan^{-1}\left(\frac{w+d}{2\ell}\right). \quad (2)$$

In Eq. (2), w is the width of the sensor, and R is the resolvable angle.

Due to manufacturing constraints at the time of the experiments, a 15-deg diffuser was used. It can be seen in Fig. 8 (middle) that the angular distribution, thus radiance, is fairly constant across the 15-deg interval when the diffuser receives a collimated input. As shown in the above calculations, the 15-deg angle is insufficient to abate beam steering in the periphery when using the light collection scheme shown in Fig. 6, where $\alpha_{max} = 9.8°$. However, by increasing the distance between the

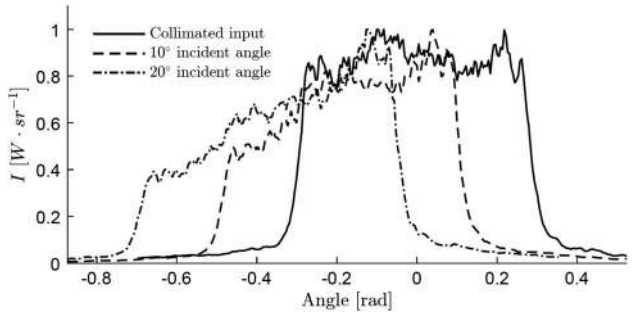

Fig. 9. Measured radiance from a 30-deg diffuser with different incident angles. A laser was used as the input with the incident angle varied. The noisy appearance of the profiles is due to speckle.

LED and Fresnel, as seen in Fig. 8 (top), slightly focusing the light to the diffuser, one can direct the illumination without degrading the angular uniformity, as seen in Fig. 8 (bottom). This enables the angular distribution to be more centered about the acceptance cone of the collection optics in the periphery, accommodating α_{max}. It is, however, recommended to dimension according to ideal diffuser behavior, as focusing the rays to the diffuser may not give the same result when using different distances and collection optics. If the incident angle to the diffuser becomes too large, the angular uniformity may suffer significantly, as can be seen in the example in Fig. 9.

5. SETUP PERFORMANCE

The performance of the DBIEI setup dimensioned according to the relations presented in Section 3 (Fig. 4) and characterized in Section 4 has been evaluated in a constant volume, pre-burn combustion vessel. This vessel is capable of creating thermodynamic conditions similar to those in a diesel engine cylinder. Injections of liquid fuel are investigated in terms of spray and combustion characteristics using various optical diagnostics [5,8,13,14,20,22–24].

The physical dimensions of the combustion vessel constraining the design of the DBIEI setup include 102-mm-diameter clear aperture side windows with an outer surface ~100 mm (optically) from the plane passing through the injector or spray/flame axis [22]. These constraints limit both the size of the diffuser (D) and distance between the diffuser and the image plane (L) to 100 mm. A Phantom v2512 high-speed CMOS camera was used for collection. As mentioned previously, a 100-mm-diameter, 15-deg diffuser was used, as this was the largest angle available at the time of this work.

The LED source was pulsed in order to reduce the duty cycle of the aforementioned Sandia-developed LED driver, thereby enabling significantly higher light intensity during the short exposure time of the camera. Over the 2-μs pulse duration used for these experiments, the LEDs were able to deliver energy levels ranging from 50 to 100 μJ, depending on the wavelength of the illumination. The performance of the optical setups shown in Fig. 10 is evaluated and compared to the modified version of the Ghandhi and Heim setup [4–6,8,15], as it has been used extensively for DBIEI-LL and DBIEI-soot measurements within the ECN community. An A Injector 0766-

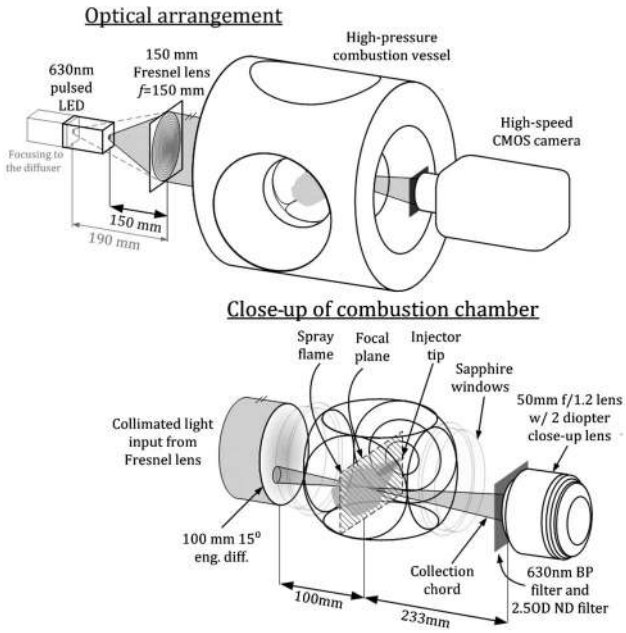

Fig. 10. Optical setup for high-temporal resolution DBIEI-LL and DBIEI-soot measurements of liquid fuel spray in high-pressure and high-temperature ambient conditions.

306-04 from the family of ECN Spray A injectors, a 90-μm orifice nozzle, was used in these experiments. The measurements with the modified Ghandhi and Heim setup were obtained with Spray A injector 210370 [25].

Results of extinction by liquid fuel droplets, τ^*, obtained with DBIEI-LL are presented in Fig. 11.

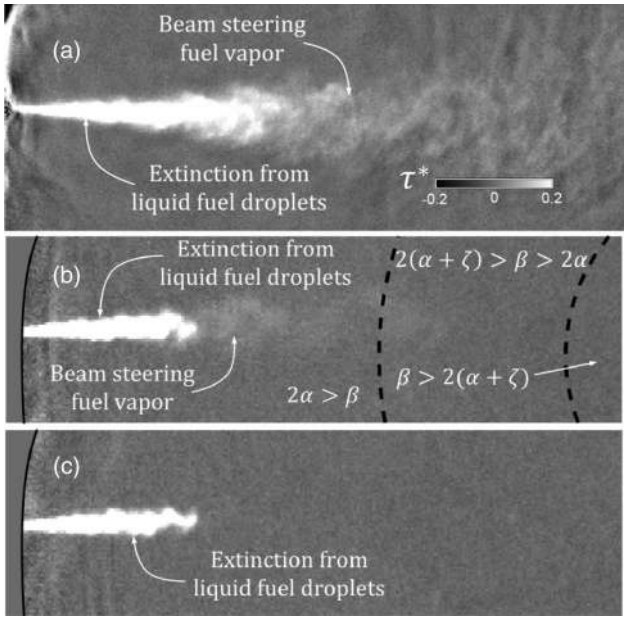

Fig. 11. Instantaneous τ images of DBIEI-LL measurement from a 90 μm orifice injector into an ambient with $T_{amb} = 900$ K and $\rho_{amb} = 22.8$ kg/m^3 using (a) modified Ghandhi and Heim setup with a 450 nm LED and 82 kHz frame rate, (b) current setup with a 623-nm LED, 15-deg diffuser, and 150 kHz frame rate, and (c) same setup with focusing to the diffuser.

It can be seen that the reduction of beam-steering artifacts increases the contrast at the liquid phase boundary in Figs. 11(b) and 11(c) compared to 11(a). This is especially true at the axial extent of the liquid where the dense fuel vapors induce a high apparent optical thickness. The apparent optical thickness in this region will be positive, as the steering is preferential due to the dense fuel vapors being cooler than the ambient.

Beam-steering artifacts are still apparent in Fig. 11(b) where $\beta < 2\alpha$, though not as pronounced as beam-steering from the flame in the regions where $\beta < 2\alpha$ as seen in Fig. 12(b). This indicates that the dense fuel vapor induces a smaller ζ than the hot flame. No beam-steering effects are apparent when slightly focusing the light to the diffuser, as demonstrated in Fig. 11(c). The suppression of the apparent optical thickness significantly reduces the uncertainties involved in determining the actual liquid penetration length, as the liquid boundary is based on a $\tau^* = 0.37$ threshold [26], corresponding to the Mie scatter standard threshold of 3% maximum Mie scatter signal [22]. Peripheral effects in the region close to the injector are evident in Figs. 11(b) and 11(c). These effects occur due to the limited optical access, such that the illumination is insufficiently extended close to the walls.

Soot extinction results, in terms of optical thickness (KL), obtained with DBIEI-soot are provided in Fig. 12. Beam-

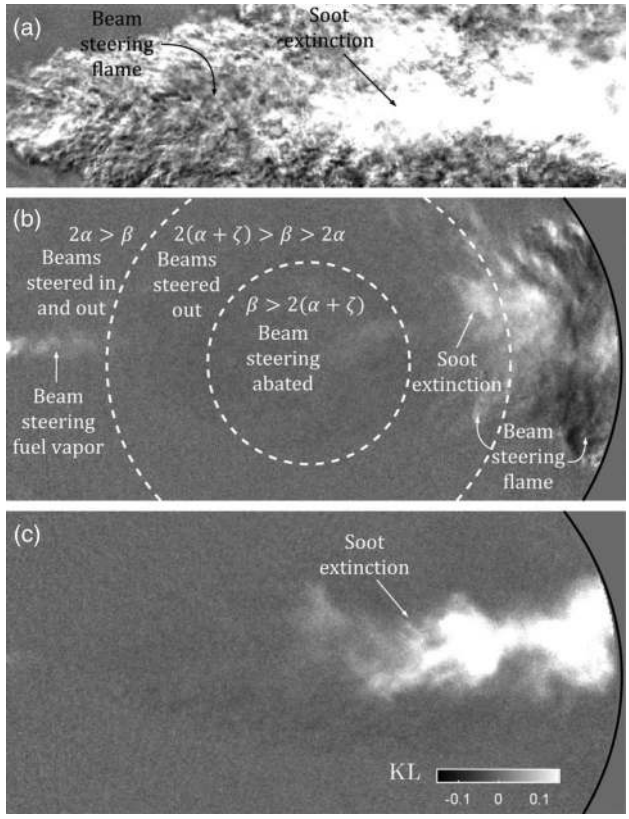

Fig. 12. Instantaneous KL images of DBIEI-soot measurement from 90 μm orifice injector into an ambient with $T_{amb} = 900$ K and $\rho_{amb} = 22.8$ kg/m^3 using, (a) modified Ghandhi and Heim setup with 623-nm LED and 41 kHz frame rate, (b) current setup with 623-nm LED, 15-deg diffuser, and 45 kHz frame rate and (c) same setup with focusing to the diffuser.

steering effects due to refractive index gradients are easily distinguishable as schlieren patterns in Fig. 12(a). The measurement using a 15-deg diffuser with a collimated input shown in Fig. 12(b) yields significant improvements. However, some beam-steering artifacts are apparent in certain regions of the image as expected due to the previously described dimensioning. Based on the measurements of the collection optics and lighting characteristics, the regions where beam-steering artifacts may result in positive and/or negative apparent optical thickness are bounded with dashed lines. The measurements are consistent, as negative optical thickness can be observed only beyond the second boundary where $\beta < 2\alpha$. With the lighting characteristics prescribed as in the bottom panel of Fig. 8, the angular distribution shifts according to the optical axis of the collection optics, thereby the expanding the boundaries, such that beam steering is eliminated in the entire image, as seen in Fig. 12(c).

In addition to introducing uncertainty to the measured optical thickness, beam-steering artifacts may affect the interpreted local soot concentration, as it is obtained through tomographic reconstruction. This procedure is very sensitive to spatial variations in the measured optical thickness.

Previous measurements used shorter wavelengths of incident light (400–550 nm) in order to enhance the KL signal-to-beam-steering ratio [6,8]. This restriction to shorter wavelengths poses further uncertainties due to the limited knowledge of the optical properties of soot in this wavelength range, the increased sensitivity to the hydrogen content from nascent to mature soot particles [27], and to scattering.

6. SUMMARY

This paper reviews a number of the techniques previously applied to image extinction in media characterized by steep refractive index gradients and presents the development of an improved illumination configuration. The previous techniques discussed here all used diffused illumination; however, none of these prior works provided detailed characterization of the lighting or analysis demonstrating how diffused illumination effectively eliminates the effects of beam steering in extinction imaging measurements. In this work, a detailed theoretical description of the lighting characteristics required to isolate extinction is given. The light source should be extended and spatially uniform with a constant radiance. Based on these characteristics, an optical setup is dimensioned to facilitate high-speed extinction imaging. The setup has been applied to measure automotive fuel sprays. By using an engineered diffuser, one can generate constant radiance illumination over a specific angular range, thereby maximizing the light throughput while still maintaining the desired lighting characteristics. This work serves as a guide for dimensioning an optical setup according to the unique limiting geometrical constraints of a user's experimental facility and provides methods to characterize both lighting and collection. The intent is to establish a standard for extinction imaging measurements submitted to the ECN and to provide ECN contributors with the information necessary to characterize an optical setup suitable for use in their respective combustion vessels. This work presents the dimensioning of a setup for the constant-volume, pre-burn combustion vessel at Sandia National Labs. Liquid and soot extinction measurements acquired with this setup demonstrate the effective elimination of beam steering when the theoretically derived illumination and collection constraints are met.

APPENDIX A

The concept of the light extinction setup is illustrated in Fig. 13(a), where only the light collection to a single pixel is shown. The marginal rays that are traced in the illustration are defined by the angular aperture of the camera objective. The marginal rays define the acceptance cone of the particular collection system to the particular pixel. The acceptance cone is assumed to be rotationally symmetric around the chief ray. A unit sphere is illustrated around the focal point to show the solid angle of the acceptance cone. The acceptance cone on the opposite side of the focal point is collecting light from an extended, spatially uniform, and planar light source.

Figure 13(b) shows a single ray within the acceptance cone to illustrate the relation between radiant flux observed, $d\Phi_{em}$, by a small area, dA_{obs}, in the focal point and radiant flux emitted, $d\Phi_{em}$, from a small area, dA_{em}, on the light source. A unit sphere is also illustrated around the center of dA_{em} to show the solid angle of light subtended by dA_{obs}. The radiance, $L_{em}(\theta)$ [$W/(m^2\,sr)$], emitted by the projected area $\cos(\theta)dA_{em}$ of the light source within the solid angle $d\Omega_{em}$ is defined as Eq. (A1):

$$L_{em}(\theta) = \frac{d^2\Phi_{em}}{\cos(\theta)dA_{em}d\Omega_{em}}. \tag{A1}$$

The radiance, $L_{obs}(\theta)$, observed by the area dA_{obs} within the solid angle $d\Omega_{obs}$ is defined as Eq. (A2):

$$L_{obs}(\theta) = \frac{d^2\Phi_{obs}}{dA_{obs}d\Omega_{obs}}. \tag{A2}$$

Since $d\Omega_{em}$ is subtended by dA_{obs} and $d\Omega_{obs}$ by dA_{em}, the solid angles depend upon the distance, x, through Eqs. (A3) and (A4):

$$\cos(\theta)dA_{em} = x^2 d\Omega_{obs}, \tag{A3}$$

$$dA_{obs} = x^2 d\Omega_{em}. \tag{A4}$$

These relations are easier understood from the illustration in Fig. 13(b), where $d\Omega_{em}$ and $d\Omega_{obs}$ are shown as projections of dA_{obs} and dA_{em}, respectively, on the opposed unit sphere. In a lossless environment, energy conservation implies that $\Phi_{em} = \Phi_{obs}$. Inserting Eqs. (A3) and (A4) into Eq. (A1), substituting Φ_{em} with Φ_{obs}, and integrating with respect to $d\Omega_{obs}$ leads to an expression for irradiance, $E = d\Phi/dA$ [Wm^{-2}]. As L_{em}/n^2 is conserved in a lossless environment, the irradiance can be expressed by the emitted radiance, provided the observer and emitter are surrounded by a medium of the same refractive index [Eq. (A5)]. Note also that the observed irradiance emitted by the extended source and independent of the distance:

$$\frac{d\Phi_{obs}}{dA_{obs}} = \int_{\Omega_{obs}} L_{em}(\theta)\mathrm{d}\Omega_{obs}. \tag{A5}$$

The irradiance is a useful quantity because the cross section area at the focal point in Fig. 13(a) is small and may be considered as $\Delta A_{obs} = dA_{obs}$. The size of ΔA_{obs} is eventually determined by the camera objective and the pixel size, and may thus be considered as a fixed value during the measurements. The radiant

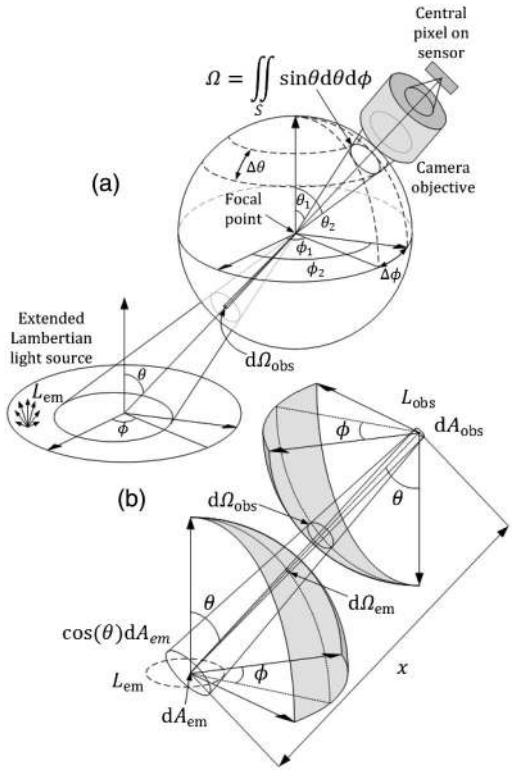

Fig. 13. Illustration of irradiance quantified through the focal point of one pixel from an extended light source with constant radiance subtended by the solid angle, Ω, of the camera objective. Also illustrated is the radiant exchange between an infinitesimal area in the focal point and an infinitesimal area on the source.

flux arriving on the pixel in Fig. 13(a) will, according to Eqs. (A3) and (A4), be independent of the distance, x, between the camera and the source, if the light source is extended and spatially uniform with a fixed angular radiance profile.

Furthermore, if the light source is Lambertian, meaning that radiance is independent of viewing angle, it follows that Eq. (A5) may be reduced to Eqs. (A6) and (A7):

$$\frac{d\Phi_{obs}}{dA_{obs}} = L_{em}\Omega_{obs}, \tag{A6}$$

$$\Phi_{obs} = L_{em}\Omega_{obs}A_{obs}. \tag{A7}$$

This states that the radiant flux detected by a pixel is also independent of the viewing angle relative to the light source and depends only on the angular aperture of the camera objective and the radiance emitted by the source [28,29].

In summation, the optical invariant and radiance theorem state that entendue, $n^2\Omega A$, and basic radiance, L/n^2, are conserved in an optical system. Thus, Eq. (A7) is valid despite variations in the refractive index between observer and emitter, provided they are immersed in surroundings with the same refractive index.

Funding. U.S. Department of Energy (DOE), Office of Energy Efficiency and Renewable Energy: Vehicle Technologies program; Danish Strategiske Forskningsråd (DSF), Technical University of Denmark, Department of Mechanical Engineering (DTU MEK); Danish Maritime Fund; Orient's Fund; Lauritzen Foundation; Torm Foundation.

Acknowledgment. C. Carlen and D. Cicone are gratefully acknowledged for technical assistance. The authors also wish to thank G. Singh and L. Breston, program managers at the U.S. DOE, for their support. Sandia National Laboratories is a multi-mission laboratory managed and operated by National Technology and Engineering Solutions of Sandia, LLC., a wholly owned subsidiary of Honeywell International, Inc., for the DOE's National Nuclear Security Administration under contract DE-NA0003525.

REFERENCES

1. H. Hovarth, "Atmospheric light absorption–a review," Atmos. Environ. **27A**, 293–317 (1993).
2. M. Musculus and L. M. Pickett, "Diagnostic considerations for optical laser-extinction measurements of soot in high-pressure transient combustion environments," Combust. Flame **141**, 371–391 (2005).
3. J. B. Ghandhi and D. M. Heim, "An optimized optical system for backlit imaging," Rev. Sci. Instrum. **80**, 056105 (2009).
4. M. Bardi, R. Payari, L. M. Malbec, G. Brunaux, L. M. Pickett, J. Manin, T. Bazyn, and C. L. Genzale, "Engine combustion network: comparison of spray development, vaporization, and combustion in different combustion vessels," Atomization Sprays **22**, 807–842 (2012).
5. J. Manin, M. Bardi, and L. M. Pickett, "Evaluation of the liquid length via diffused back-illumination imaging in vaporizing diesel sprays," in *Proceedings of the 8th International Conference on Modeling and Diagnostics for Advanced Engine Systems, COMODIA 2012* (2012).
6. J. Manin, L. M. Pickett, and S. A. Skeen, "Two-color diffused back-illumination imaging as a diagnostic for time-resolved measurements in recting sprays," SAE Int. J. Engines **6**, 1908–1921 (2013).
7. R. Payri, F. J. Salvador, P. M. Aldaraví, and D. Vaquerizo, "ECN Spray G external spray visualization and spray collapse description through penetration and morphology analysis," Appl. Therm. Eng. **112**, 304–316 (2017).
8. S. A. Skeen, J. Manin, K. Dalen, and L. M. Pickett, "Extinction-based imaging of soot processes over a range of diesel operating conditions," in *8th U.S. National Combustion Meeting*, Salt Lake City, Utah (2013).
9. J. Pastor, J. Garcia-Oliver, R. Novella, and T. Xuan, "Soot quantification of single-hole diesel sprays by means of extinction imaging," SAE Int. J. Engines **8**, 2068–2077 (2015).
10. J. Sjöholm, R. Wellander, H. Bladh, M. Richter, P. E. Bengtson, M. Alden, U. Aronson, C. Chartier, Ø. Andersson, and B. Johansson, "Challenges for in-cylinder high-speed two-dimensional laser-induced incandescence measurements of soot," SAE Int. J. Engines **4**, 1607–1622 (2011).
11. I. G. Boxx, O. Heinold, and K. P. Geigle, "Laser-induced incandescence measurements in a fired diesel engine at 3 kHz," Exp. Fluids **56**, 3 (2015).
12. P. Bakker, R. Willems, and N. Dam, "Implementation of high-speed laser-induced incandescence imaging in CI engines," SAE Technical Paper 2016-01-0725 (2016).
13. L. M. Pickett and D. Siebers, "Fuel effects on soot processes of fuel jets at DI diesel conditions," SAE Technical Paper 2003-01-3080 (2003).
14. L. M. Pickett and D. L. Siebers, "Soot in dieselfuel jets: effect of ambient temperature, ambient density, and injection pressure," Combust. Flame **138**, 114–135 (2004).
15. L. M. Pickett, J. Manin, and C. L. Genzale, "Uncertainty quantification for liquid penetration of evaporating sprays at diesel-like conditions," Atomization Sprays **25**, 425–452 (2015).

16. P. S. Greenberg and J. C. Ku, "Soot volume fraction imaging," Appl. Opt. **36**, 5514–5522 (1997).
17. Y. Xu and C. F. Lee, "Forward-illumination light-extinction technique for soot measurement," Appl. Opt. **45**, 2046–2057 (2006).
18. K. A. Thomson, M. R. Johnson, D. R. Snelling, and G. J. Smallwood, "Diffuse-light two-dimensional line-of-sight attenuation for soot concentration measurements," Appl. Opt. **47**, 694–703 (2008).
19. C. Carlen, "High speed, high current pulsed driver circuit," U.S. patent 14/998,101 (21March 2015).
20. J. Manin, M. Bardi, L. M. Pickett, R. N. Dahms, and J. C. Oefelein, "Microscopic investigation of the atomization and mixing processes of diesel sprays injected into high pressure and temperature environments," Fuel **134**, 531–543 (2014).
21. R. E. Jacobson, S. F. Ray, G. G. Attridge, and N. R. Axford, *The Manual of Photography*, 9th ed. (Focal, 2000).
22. D. L. Siebers, "Liquid-phase fuel penetration in diesel sprays," SAE Technical Paper 980809 (1998).
23. S. A. Skeen, J. Manin, L. M. Pickett, K. Dalen, and A. Ivarsson, "Quantitative spatially resolved measurements of total radiation in high-pressure spray flames," SAE Technical Paper 2014-01-1252 (2014).
24. S. A. Skeen, J. Manin, and L. M. Pickett, "Simultaneous formaldehyde PLIF and high-speed schlieren imaging for ignition visualization in high-pressure spray flames," Proc. Combust. Inst. **35**, 3167–3174 (2015).
25. A. L. Kastengren, F. Z. Tilocco, C. F. Powell, J. Manin, L. M. Pickett, R. Payri, and T. Bazyn, "Engine combustion network (ECN): measurements of nozzle geometry and hydraulic behavior of diesel sprays," Atomization Sprays **22**, 1011–1052 (2012).
26. L. M. Pickett, C. L. Genzale, J. Manin, and L. M. Malbec, "Measurement uncertainty of liquid penetration in evaporating diesel sprays," in *23rd Annual Conference on Liquid Atomization and Spray Systems* (2011).
27. R. C. Millikan, "Optical properties of soot," J. Opt. Soc. Am. **51**, 698–699 (1961).
28. W. McCluney, *Introduction to Radiometry and Photometry*, 2nd ed. (Artech House, 2014).
29. H. C. Hottel and A. Sarofim, *Radiative Transfer* (McGraw-Hill, 1967).